Chapter 9
Wireless Actuation of Micro/Nanorobots for Medical Applications

Soichiro Tottori, Li Zhang, and Bradley J. Nelson

9.1 Introduction

People have envisioned tiny robots that can explore a human body, find and treat diseases since Richard Feynman's famous speech, "There's plenty of room at the bottom," in which the idea of a "swallowable surgeon" was proposed in the 1950s [1]. Even though we are at a state of infancy to achieve this vision, recent intense progress on nanotechnology and micro/nanorobotics has accelerated the pace toward the goal [2–6]. A number of research efforts have been recently published regarding the development from the basic principles and fabrication methods to practical applications [7–10]. Not limited in vivo applications, the integration of micro/nanorobots to lab-on-a-chip systems can also be foreseen because of the nature of their size and liquid operating environments [11, 12]. This interdisciplinary research of micro/nanorobot-based medical treatments or diagnosis has been investigated from many different aspects, such as locomotion, functionalization, imaging, biocompatibility, interface, etc (Fig. 9.1). In this chapter we focus on wireless actuation of micro/nanorobots, which plays an important role in locomotion and part of functionalization. The chapter starts from wireless locomotion by means of magnetic fields, bacteria, and chemical reaction, followed by wireless actuation of robotic tools that function to manipulate targets.

S. Tottori • B.J. Nelson (✉)
Institute of Robotics and Intelligent Systems, ETH Zurich, 8092 Zurich, Switzerland
e-mail: bnelson@ethz.ch

L. Zhang
Department of Mechanical and Automation Engineering, The Chinese University of Hong Kong, Shatin NT, Hong Kong, SAR, China

Y. Ge et al. (eds.), *Nanomedicine*, Nanostructure Science and Technology,
DOI 10.1007/978-1-4614-2140-5_9

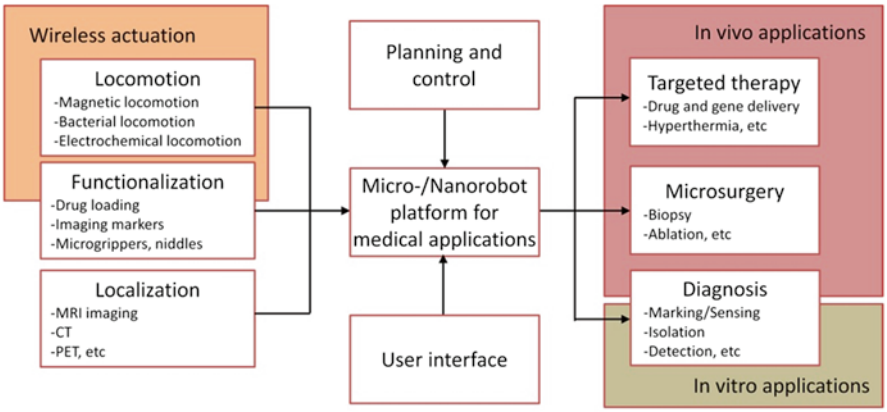

Fig. 9.1 A road map of micro/nanorobots for medical applications

9.2 Magnetic Actuation

Safety issues with respect to transmitting energy through body tissues and biocompatibility of the wirelessly driven device must be taken into account for in vivo applications. As MRI systems have been used extensively in clinical practice, it is accepted that the limited strength and frequency of these magnetic fields are safe. Therefore, magnetic actuation is one promising approach for powering and manipulating medical micro/nanorobots in vivo. Moreover, the human body is magnetically transparent, which implies that interference of magnetic fields by human bodies is practically negligible.

In general, magnetic actuation can be categorized into two types: force-driven and torque-driven. Magnetic attraction forces are generated by gradient fields, whereas magnetic torques are generated by misalignment of magnetizations of the devices and magnetic fields. Using the average magnetization **M** of the magnetic body in Amps per meter (A m^{-1}), the magnetic force and torque are described, respectively, as:

$$\mathbf{F} = V\left(\mathbf{M} \bullet \nabla\right)\mathbf{B} \tag{9.1}$$

and

$$\mathbf{T} = V\mathbf{M} \times \mathbf{B} \tag{9.2}$$

where V is the volume of the body, and **B** is the flux density of an external field in Tesla (T).

9.2.1 *Gradient Field for Concentration and Steering of Magnetic Therapeutic Carriers*

As described in Eq. 9.1, magnetic carriers are attracted to the direction of the high flux density of gradient fields. Magnetic nanoparticles are widely used to magnetically-tag therapeutic carriers [13, 14]. The approach of using gradient fields to move magnetic therapeutic carriers can be further divided, depending on the applied magnetic systems, into the following three groups: concentration using permanent magnets placed outside the body, direct concentration at implants, and steering of magnetic carriers in flows using the MRI system.

9.2.1.1 Concentrating Magnetic Carriers at Targeted Sites by External Magnets

Concentration of magnetic carriers using permanent magnets or electromagnets is probably the most straightforward method of using magnetic-field-based manipulation. Figure 9.2a shows that a strong magnet is placed on the surface or incised region of a patient body, and the magnetic therapeutic carriers flowing in the circulatory system are trapped in a local region by magnetic attraction [13, 16]. This approach has been investigated for treatment of tumors located at various sites in vivo, such as livers [17, 18], brains [19, 20] and lungs [15].

In Dames et al. [15], Rudolph and coworkers demonstrated that magnetic aerosols that contain superparamagnetic iron oxide nanoparticles (SPIONs) can be collected by external electromagnets in mouse lungs. The single SPIONs themselves do not have sufficient magnetization to be attracted by a gradient field, however, the magnetic aerosols (~3.5 μm) containing approximately 2,930 SPIONs can be guided in a high magnetic flux gradient (larger than 100 T m^{-1}). Figure 9.2b shows that SPIONs were collected in the right lung, as the magnet's tip was located directly above the right lung lobe, surgically exposed by thoracotomy. Figure 9.2c and d are histological images of right and left lungs, respectively, in which the brown areas show the accumulated SPIONs. The magnetic aerosol can also contain several different drugs, biodegradable nanoparticles, liposomes, nanocrystals and so on. The major challenge for scaling up from mouse to human size is generation of large magnetic gradient fields to a relatively far location from the tip of the electromagnet core.

9.2.1.2 Concentrating Magnetic Therapeutic Carriers Directly at Implants

An alternative approach to concentrate magnetic particles in vivo is proposed by using magnetic implants with an externally applied uniform field. Externally applied uniform fields induce magnetization of magnetic implants and flowing magnetic therapeutic carriers simultaneously. Gradient fields are generated surrounding the

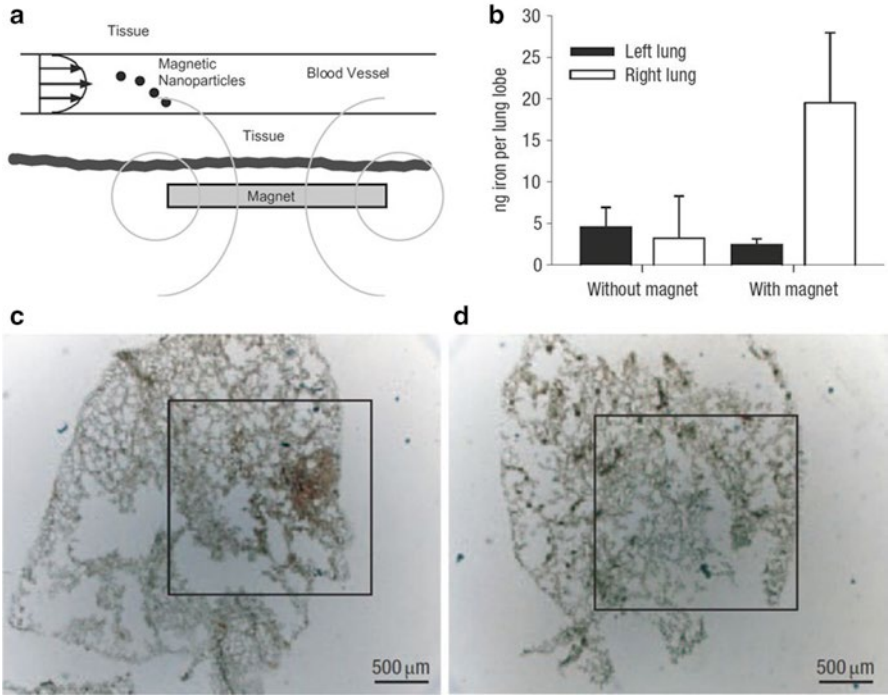

Fig. 9.2 Concentration of magnetic therapeutic carriers. (**a**) Schematic illustration of capturing magnetic therapeutic carriers: a magnet is place outside or an incised region in order to collect magnetic therapeutic carriers flowing in the circulatory system ((**a**) Reprinted with permission from Pankhurst et al. [14]. Copyright 2003 IOP Publishing Ltd.) (**b**) The bar graph shows the amount of SPION in the *left* (without a magnetic field) and *right* (with a magnetic field) lungs (thoracotomy, 400 breathing cycles, ~300 μl SPION solution, 12.5 mg ml^{-1} Fe, $n = 3 \pm$ s.d.). (**c–d**) Lung histology after nanomagnetosol application. (**c**: right lung, **d**: left lung) ((**b–d**) Reprinted with permission from Dames et al. [15], Copyright 2007 Macmillan Publishing Ltd: Nature Nanotechnology)

ferromagnetic implants because the implants possess much higher magnetic permeabilities than that of air and bodily tissues. In comparison to the method described in the last section, i.e. direct use of gradient fields generated by external magnets, the method using magnetic implants can provide relatively strong gradient fields, because the source of gradient is installed at the targeted site inside the body [21]. Based on this concept, targeting of magnetic therapeutic carriers at the implanted sites has been demonstrated to deliver drugs or cells [22–26].

In Polyak et al. [26], Levy and co-workers demonstrated targeting delivery of magnetic nanoparticle-loaded endothelial cells to the stent surface, as illustrated in Fig. 9.3a. They applied the magnetic stents made from 304-grade stainless steel instead of conventional non-magnetic medical-grade stainless-steel 316 L. The bovine aortic endothelial cells (BAECs) functionalized with magnetic nanoparticles were accumulated onto the magnetic stents in the uniform field. In vivo acute rat

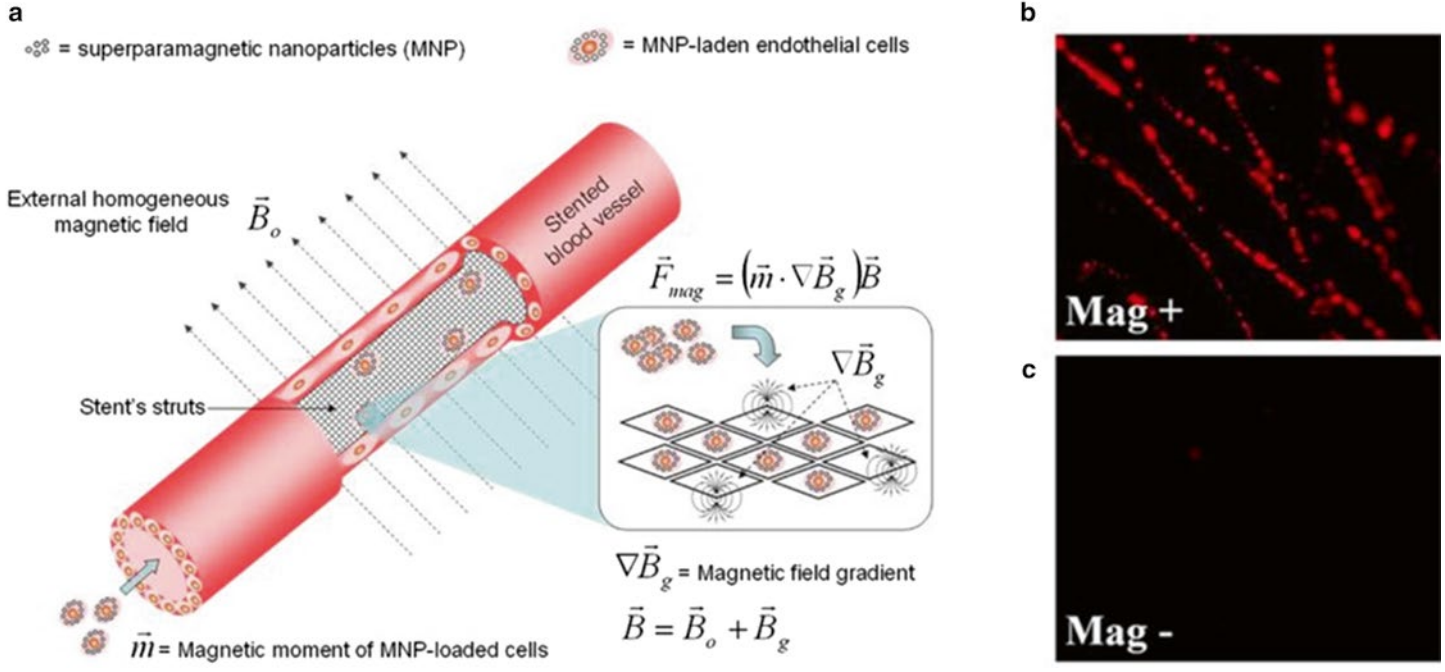

Fig. 9.3 Localizing magnetic therapeutic carriers around magnetic implants using uniform magnetic field. (**a**) Schematic illustration of MNP-laden endothelial cells attracted to the magnetic stent in the presence of a uniform magnetic field. (**b**, **c**) In vivo experiment of MNP-loaded BAECs capturing on the implanted stents. BAECs preloaded with fluorescent MNPs were tranthoracically injected into the left ventricular cavity. The uniform magnetic field of 100 mT was applied for 5 min. (**b**) Fluorescent image of the MNP-laden BAECs accumulated on the stent implanted in the rat carotid artery. (**c**) Control experimental results without magnetic fields ((**a**–**c**) Reprinted with permission from Polyak et al. [26]. Copyright 2008 National Academy of Science U.S.A.)

carotid stenting studies were performed by transthoracic injection of MNPs-loaded (MNP: magnetic nanoparticle) BAECs into the left ventricular cavity of the rat. Figure 9.3b and c show the fluorescent images of MNPs collected onto the 304-grade stainless steel stents with and without the uniform magnetic field, respectively. Clearly, the MNPs were collected on the surface of the stent in the presence of magnetic fields.

9.2.1.3 Steering Magnetic Therapeutic Carriers in Flows by MRI Systems

Using MRI systems to steer magnetic therapeutic carriers flowing in the circulatory systems is one of the emerging areas of magnetic control [27]. Localization of magnetic therapeutic carriers using permanent magnets is limited to the organs that are close to the skin because magnetic gradient fields decay rapidly as the distance between the target and the externally placed magnets increases. The gradient field provided by a MRI system is appealing for steering magnetic therapeutic carriers deep inside the body because of its gradient linearity, high-strength and real-time imaging feedback.

The MRI-system-based steering of magnetic therapeutic carriers in bifurcations in vitro and in vivo has been reported recently [28–31]. For example, in Pouponneau et al. [30] Martel and co-workers demonstrated in vivo guidance of magnetic therapeutic carriers for the treatment of hepatocellular carcinoma (HCC) via trans-arterial chemoembolization in the hepatic artery using rabbits. Figure 9.4a and b show that the magnetic therapeutic carriers: biodegradable polymer particles containing anti-tumor drug and magnetic nanoparticles were steered in the hepatic arterial bifurcation in the presence of a gradient field. In Fig. 9.4c, the result shows that the deposition of magnetic therapeutic carriers in the targeted and untargeted lobes were increased and decreased by MRI steering, respectively. In Fig. 9.4d, the magnetic therapeutic carriers, visualized as dark spots in MR images, were collected in the left lobe. The histological image in Fig. 9.4e shows that magnetic therapeutic carriers were deposited within a branch of the hepatic artery.

9.2.2 Magnetic-Torque-Driven Propulsion at Low Reynolds Number

Locomotion of micro/nanorobots in a fluidic environment at low Reynolds number is challenging, since viscosity dominates over inertia [32, 33]. A scallop-like motion, one of the typical examples of reciprocal motions, cannot get net forward displacement but just moves forward and backward repeatedly at the same place in a low Reynolds number regime because the flow is time-reversible. In nature, microorganisms utilize various non-reciprocal locomotion strategies. For example, spermatozoa propel themselves by propagating a wave motion on their flexible tails, and *E. coli* bacteria swim by rotating their helical flagella.

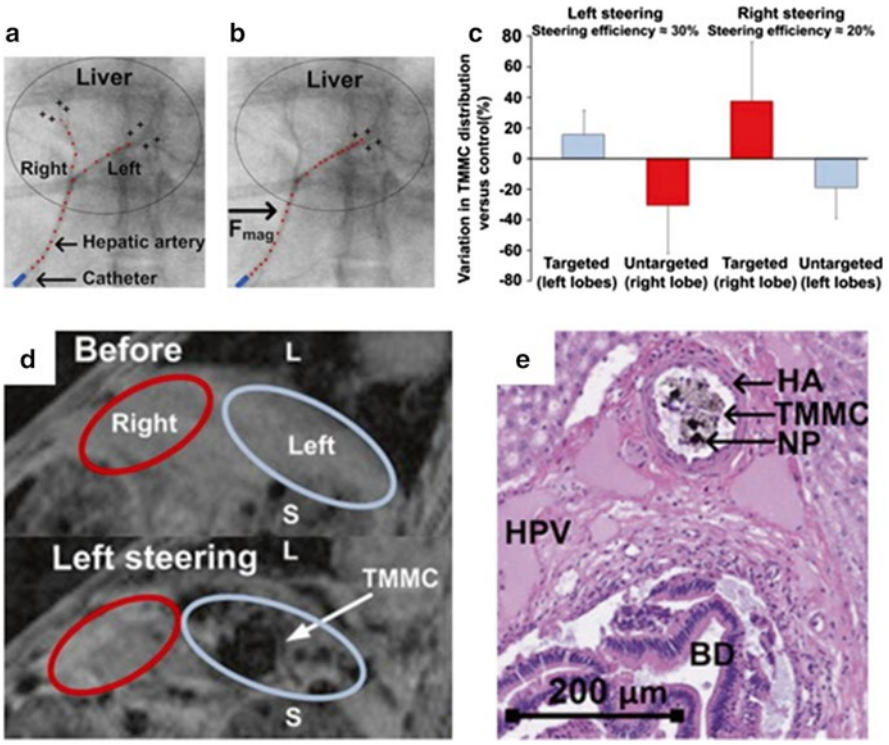

Fig. 9.4 Steering magnetic therapeutic carriers for liver chemoembolization using an upgraded MRI system. (**a**, **b**) Fluoroscopy images of the rabbit hepatic artery with superposed images of the magnetic therapeutic carriers without (**a**) and with (**b**) the MRI control. (**a**) The microparticles are released from the catheter in the artery and distributed to both lobes. (**b**) MRI steering of magnetic therapeutic carriers to left lobe to preserve the right lobe from the chemoembolization. (**c**) Variation in TMMC (therapeutic magnetic microcarriers) distribution versus control in the liver lobes with left and right steering based on Co analysis. Mean ± SD. (**d**) T2*-weighted MR images of the rabbit liver before and after the operation. The red and blue lines indicate the right and left lobe, respectively. "S" indicates the stomach and "L" the lung. (**e**) Histological image of liver parenchyma and the blood vessels dyed with hematoxylin and eosin. HA: branch of hepatic artery, HPV: hepatic portal vein, BD: bile duct, NP FeCo nanoparticles ((**a**–**e**) Reprinted with permission from Pouponneau et al. [30]. Copyright 2011 Elsevier Ltd)

Inspired by the above mentioned microorganisms, many microscopic artificial swimmers have been developed [34–44]. For example, artificial microswimmers with traveling wave-induced propulsion were presented by Dreyfus and co-workers in Dreyfus et al. [34]. Figure 9.5a and b show the illustration and optical microscope image of the microscopic swimmer consisting of a chain of colloidal magnetic particles connected by DNA linkages, respectively. Oscillating magnetic fields induce a wave motion into the flexible body, resulting in a net forward movement. Inspired by helical bacterial flagella, artificial bacterial flagella (ABFs) consisting of ferromagnetic Ni heads and rolled-up helical tails were reported by our group elsewhere

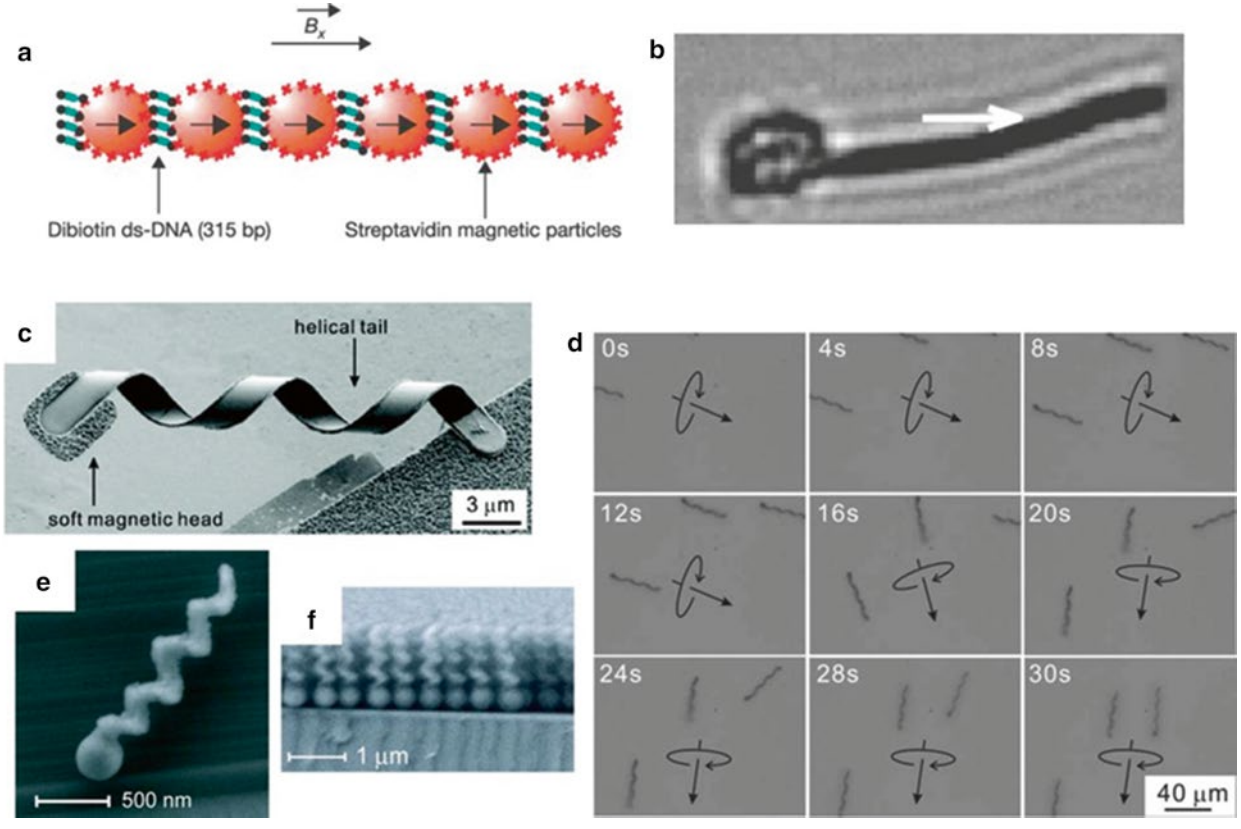

Fig. 9.5 Propulsion of non-reciprocal motions created by a oscillating or a rotating field. (**a**) Schematic representation of a flexible magnetic filament. (**b**) Optical microscopy image of the microscopic artificial swimmer. The white arrow indicates the direction of an external field ((**a**, **b**) Reproduced with permission from Dreyfus et al. [34]. Copyright 2005 Nature Publishing Group). (**c**) Helical microswimmer comprised of the magnetic head and the rolled-up helical tail. (**d**) Steering of the three ABFs as an entity ((**c**, **d**) Reproduced with permission from Zhang et al. [43]. Copyright 2009 American Chemical Society). (**e**) The microscopic helical swimmer fabricated with GLAD technique. (**f**) A wafer section with a nanostructured film after GLAD of SiO_2 helices ((**e**, **f**) Reproduced with permission from Ghosh and Fischer [37]. Copyright 2009 American Chemical Society)

[42, 43]. Figure 9.5c shows the SEM image of an as-fabricated ABF with a diameter of 2.8 μm and a length of approximate 25 μm. The top-down fabrication process of the ABFs is based on the self-rolling technique: curling generated by the stress releasing of multilayered nanoribbons [45, 46]. By applying a rotating magnetic field, the ABFs were rotated in sync with the external field rotation, resulting in a forward displacement. Swimming of the multi-agent ABFs was also demonstrated, in which the group was controlled as a single entity, as shown in Fig. 9.5d. In Ghosh and Fischer [37], Fischer and Ghosh reported an alternative fabrication approach of helical swimmers using glancing angle deposition (GLAD) of chiral structures, as shown in Fig. 9.5e. GLAD method provides porous thin films with engineered structures, such as straight pillars, zigzags structures, and helices [47]. The SEM image in Fig. 9.5f shows as-fabricated vertical array of SiO_2 helical nanostructures on self-assembled silica beads with a diameter of 200–300 nm, which had an ultra-high density of – 10^9 helices per cm^2. The helical nanostructures were released by sonication and subsequently were coated with a 30-nm thick Co thin film by evaporation. In order to generate a corkscrew motion, the helical devices were also actuated in a weak strength (6 mT) rotating magnetic field. The maximum swimming speed of approximately 40 μm/s (20 body-lengths per second) was reported. The helical swimming microrobots can also be utilized to manipulate microobjects with or without a physical contact [41, 44, 48, 49]. Once functionalized by liposomes loaded with chemical or biological substances, these helical devices have the potential to perform targeted delivery of energy and controlled drug releasing in vivo. Previously SiO_2 helical devices coated with a fluorophore were demonstrated as a proof of concept [37].

9.2.3 *Scaling Effects of Micro/Nanorobots Driven by Magnetic Force and Torque*

Stokes flow is the flow at very low Reynolds number ($Re << 1$), which indicates the ratio of inertia and viscous forces. For instance, the drag force and torque of a sphere in Stokes flow are given by

$$\mathbf{F}_{\mathbf{drag}} = 3\pi\mu d\mathbf{U} \tag{9.3}$$

and

$$\mathbf{T}_{\mathbf{drag}} = \pi\mu d^3\Omega \tag{9.4}$$

where d is the diameter of the sphere, $\mathbf{U}$ is the translational velocity, and $\mathbf{\Omega}$ is the angular velocity of the rotating sphere. Comparing with Eqs. 9.1 and 9.2, in which both magnetic force and torque are directly proportional to the volume of the magnetic body (for a sphere, i.e. $\pi d^3/6$), the maximum velocity and angular velocity by applying a gradient field and a uniform rotating field can be computed. The

translational velocity **U** of a sphere induced by a gradient pulling is proportional to the term of d^2, whereas the angular velocity **Ω** by a uniform rotating field is independent of d. Therefore, when the robots are scaled-down, with the same applied field, the translational velocity will reduced rapidly, whereas the angular velocity can be maintained as a constant. This calculations also implies that if a rotational motion can be converted to a translational motion with a converting ration of less than d^2, the corkscrew locomotion based on rotational motions can be more efficient than that based on direct translational pulling using a gradient field [50].

The propelling motion of helical swimmers is described with the force f, torque τ, angular velocity ω, and translational velocity v as Purcell [33],

$$\begin{bmatrix} f \\ \tau \end{bmatrix} = \begin{bmatrix} A & B \\ B & C \end{bmatrix} \begin{bmatrix} v \\ \varpi \end{bmatrix} \tag{9.5}$$

where the parameters A, B and C are given by geometrical parameters of a helix and the viscosity of environmental fluid [50, 51]. Since the parameters A, B and C are directly proportional to the terms L, L^2 and L^3 (here, L is the characteristic length of the helix) respectively, the velocity v is computed to be proportional to the characteristic length L. In comparison to the fact that the velocity induced by direct pulling is proportional to the second power of its characteristic length, the helical propulsion is more feasible for small scale locomotion due to the scaling effect.

9.3 Bacterial Actuation

Bacteria, as natural "microrobots," can perform robotic tasks with high intelligence. In nature, bacteria can respond to various environmental cues, for example, magnetic field (magnetotaxis), light (phototaxis), electric field (galvanotaxis), chemical concentration (chemotaxis), and heat (thermotaxis). Here we show two examples of micromanipulation using bacteria based on their magnetotaxis and phototaxis.

Magnetotactic bacteria (MTBs), which possess flagella and magnetosome, swim in the direction of a magnetic field [52]. In Martel et al. [53], Martel and coworkers demonstrated that the magnetic steering of MTBs, and explained that their motion can be potentially trackable by a clinical MRI system. Figure 9.6a and b show controlled swimming of a MTB in the presence of an external magnetic field with and without a cargo [54]. Martel's group also demonstrated micromanipulation using a swarm of MTBs, by which large thrust force can be generated for pick-and-place microobjects [56].

Using phototactic bacteria enables light control of micro/nanorobotic components [55, 57]. In Weibel et al. [55], Whitesides and co-workers demonstrated pick-and-place manipulation of micro cargos by phototaxis of bacteria and photoreactive chemical linkages. Figure 9.6c shows phototaxis of *Chlamydomonas reinhardtii* (*CR*) under LED lights. In order to transport microscale cargo, chemical

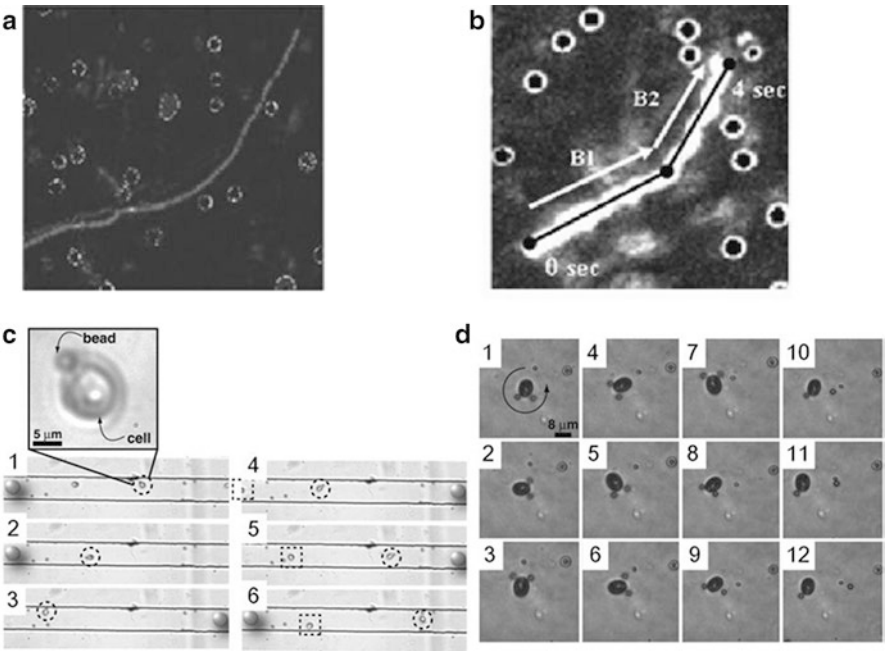

Fig. 9.6 Bacterial actuation. (**a**) Movement path of the MTB without cargos steered by an external field. (**b**) The single MTB pushed the 3-μm-diameter microbead with a control of external field. The white arrows B1 and B2 represent the direction of the field, and the black line indicates the path of microbead transported by the MTB. Images have edges of 36.0 μm ((**a**, **b**) Reproduced with permission from Martel et al. [54]. Copyright 2006 American Institute of Physics). (**c**) A sequence of images showing how the cell in C can be steered by using positive phototaxis. Illuminated LEDs are indicated by the presence of a cartoon of the LED. (**d**) A series of chronological images showing the photochemical release of a bead from a cell with two PS beads (3 μm diameter) attached by exposing UV light (λ = 365 nm, 80 W) for 20 s. The arrow in frame 1 indicates the direction in which the cell is rotating. The time that had elapsed between the frames was 2 s. In (d9), the bead was released from the cell and slowly diffused away ((**c**, **d**) Adapted with permission from Weibel et al. [55]. Copyright 2005 National Academy of Science, U.S.A.)

links were formed between cargos and *CR* bodies. The attached-cargos can be photochemically released by exposing a UV light of a specific wavelength. Figure 9.6d shows the optical microscope image of photochemical releasing of the attached microbead from *CR* by illuminating the UV light.

9.4 Chemical-Fuel-Driven Actuation

Like biomotors, such as myosins, kinesins, and dyneins, utilize ATP as chemical fuels, manmade micro/nanomotors that propel themselves by employing chemical fuels have been developed for about a decade. The first bimetal nanomotors were

demonstrated by two groups independently, one from Pennsylvania State University [58] and the other from University of Toronto [59] in 2004. A number of excellent reviews published recently regarding catalytic nanomotors from their fabrication, consideration of materials, and functionalization to their practical applications [60–63]. Here, we introduce the basic principle and some recently reported biomedical applications of these chemical-fuel-driven micro/nanomotors.

9.4.1 Principle and Fabrication

To date self-propelled micro/nanomotors exhibit locomotion in two types: bubble-induced propulsion and self-electrophoretic motion, as shown in Fig. 9.7a. The bubble-induced propulsion is based on the oxygen bubbles generated in decomposition of hydrogen peroxide. The tubular micro/nanomotors with asymmetric open ends, with conical channel, lead the bubbles emitted from the largely-opened ends. The conical microengines can be fabricated with self-rolling technique or template-assisted electroplating. The self-electrophoretic motion occurs with multisegment nanorods integrated with Au-Pt bimetals. The hydrogen peroxide is oxidized at the platinum segment, and the generated electrons travel to the gold segment, where reduction reaction occurs. Because of this asymmetrical redox reaction, the nanorods with Au-Pt bisegments move toward the direction of platinum segments. Ni segments are often integrated for steering by an external magnetic field. The multi-segmented nanorods are synthesized into the templates with cylindrical nanopores using template-assisted electrodeposition.

9.4.2 Applications

The chemical-fuel-driven micro/nanomotors can reach extremely high speeds, up to approximately 3 mm/s [67], thus the thrust force is sufficient to transport microobjects. Figure 9.7b shows transport and assembly of magnetic microplates using a microtubular motor [64]. Controlled manipulation of animal cells, i.e. CAD cells (cathecolaminergic cells), was also demonstrated, as shown in Fig. 9.7c [65]. To realize stable and selective pick-and-place manipulation, ferromagnetic layers can be integrated into the motor and the cargo for magnetic attraction [68, 69]. Releasing of the magnetic cargo is possible by turning the magnetic motor with a high speed, which is attributed to the different drag force applied on the motor and the cargo. Alternatively, UV lights can trigger photochemical releasing of the streptavidin-coated polystyrene cargo from the catalytic nanomotor [70], which is the same concept with the photochemical release of cargos from *CR* bacteria in Weibel et al. [55].

Surface-functionalized micro/nanomotors are applied for isolation of targeted biological samples, such as circulating tumor cells [71], nucleic acid [66], proteins [72], and bacteria [73], from raw complex biological media [11]. Figure 9.7d1

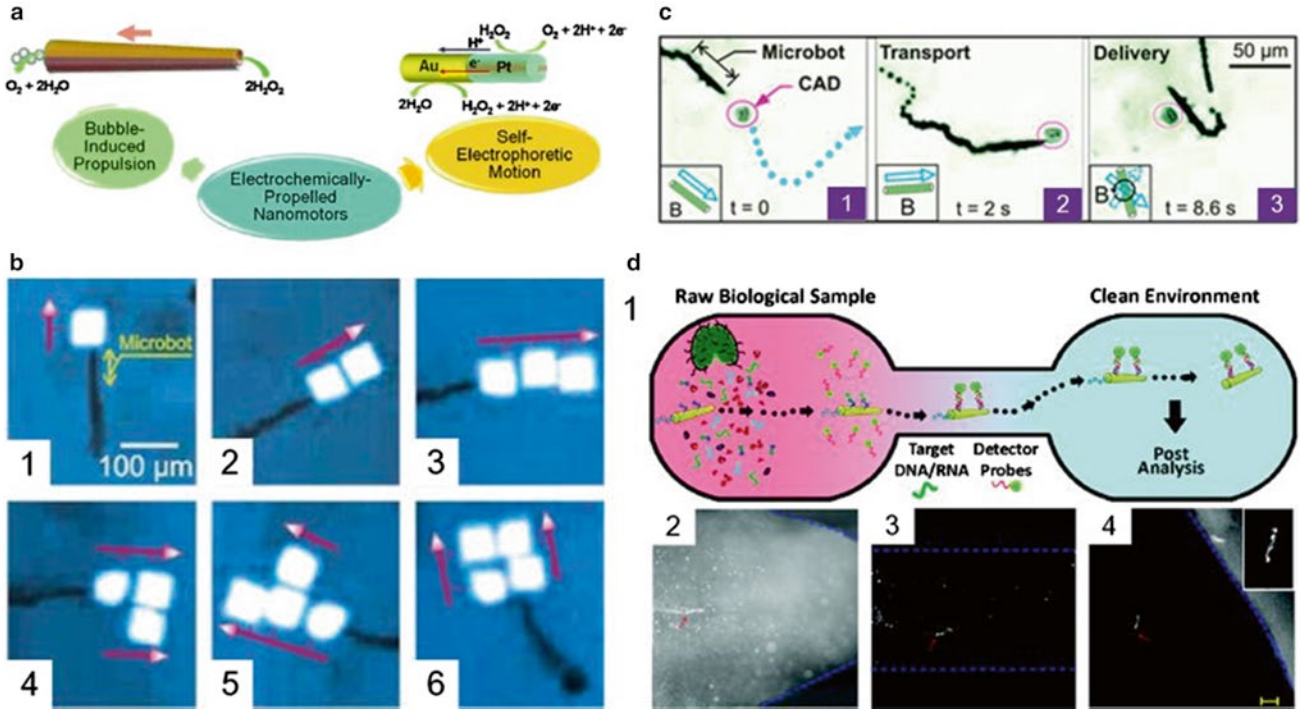

Fig. 9.7 Electrochemically-powered nanomotors. (**a**) Two types of electrochemically-powered nanomotors and their motion mechanism: bubble-induced propulsion by conical tubes and self-electrophoretic motion by bisegment rods ((**a**) Reproduced with permission from Campuzano et al. [11]. Copyright 2011 The Royal Society of Chemistry). (**b**) The catalytic microrockets assembling four magnetic plates in different configurations ((**b**) Adapted with permission from Solovev et al. [64]. Copyright 2010 John Wiley and Sons). (**c**) Controlled manipulation of CAD cells by a catalytic microrocket ((**c**) Adapted with permission from Sanchez et al. [65]. Copyright 2011 The Royal Society of Chemistry). (**d1**) Schematic illustration of isolating nucleic acid by a modified microrocket from a raw sample (*left*) to a clean/separate location (*right*). (**d2–d4**) Optical microscopy images of the modified microrocket (*red arrow*) captured the targeted DNA (**d2**) and transported it across a 6-mm-long channel (**d3**) to the clean well (**d4**) ((d) Adapted with permission from Kagan et al. [66]. Copyright 2011 American Chemical Society)

shows the schematic illustration of nucleic acid isolation by using functionalized motor from a raw biological sample to a clean microwell [66]. The outer surface of the microtubular motor was coated with a gold layer and modified with a binary self-assembled monolayer (SAM) of specific thiolated capture probe (SHCP) and a short-chain 6-mercapto-1-hexanol (MCH). The functionalized micromotors were then driven in the mixture of hydrogen peroxide and a biological sample that contains the nucleic acid (synthetic 30-mer DNA or bacterial 16S rRNA) tagged with fluorescent nanoparticles for optical visualization. Figure 9.7d2–d4 shows the optical microscopy images of capturing and transporting the targeted nucleic acids to the clean well using a micromotor.

Chemical-fuel-driven motors can also be applied for sensing based on the velocity change of their motion: the speed increases in high concentration of Ag ions in the hydrogen peroxide fuel [74]. The detection of nucleic acid was as well demonstrated by combining Ag nanoparticle-tagged detector probe [75].

To date in vivo application of chemical-fuel powered nanomotors is rare unless the current chemical fuels (mainly H_2O_2) can be replaced with biocompatible chemicals or chemicals which are inherently contained in the human body. Previously, as a proof-of-concept, bioelectrochemical motor driven by oxygen and glucose were reported [76].

9.5 Wirelessly-Actuated Robotic Tools

One of the next steps from wireless locomotion is wireless manipulation, such as holding, pinching, penetrating, etc, using nano-/microrobots. Variety of fabrication methods have been investigated and applied to create such functional wireless micro/nanorobots [77]. In this section, we explain some examples of recently reported fabrication methods and the wirelessly-actuated microrobotic tools developed with these method.

The microholders with comparable sizes enable pick-and-place manipulation of cargos without dropping off during transportation. In Tottori et al. [41], the crawlike structures were implemented at one end of the helical micromachines. The SEM image of as-fabricated functionalized micormachine is shown in Fig. 9.8a. The structures were fabricated by means of three-dimensional lithography, in which the focused UV laser is scanned in the thin layers of photocurable polymer. In comparison to the conventional two-dimensional lithography, three-dimensional lithography provides almost arbitrary shapes with a submicron resolution. The combination of electron beam evaporation of ferromagnetic thin films allows magnetic wireless actuation of the devices. The functionalized helical micromachines were capable of transport polystyrene microbeads not only horizontally but also against gravity. The process is divided into the following four stages: approaching, loading, transporting, and releasing, as illustrated in Fig. 9.8b. A polystyrene microparticle with a diameter of 6 μm was transported in three dimensions above the Si substrate with two different heights, as shown in Fig. 9.8c. The loading and releasing of the microparticle were realized by pushing it forward and swimming backward, respectively.

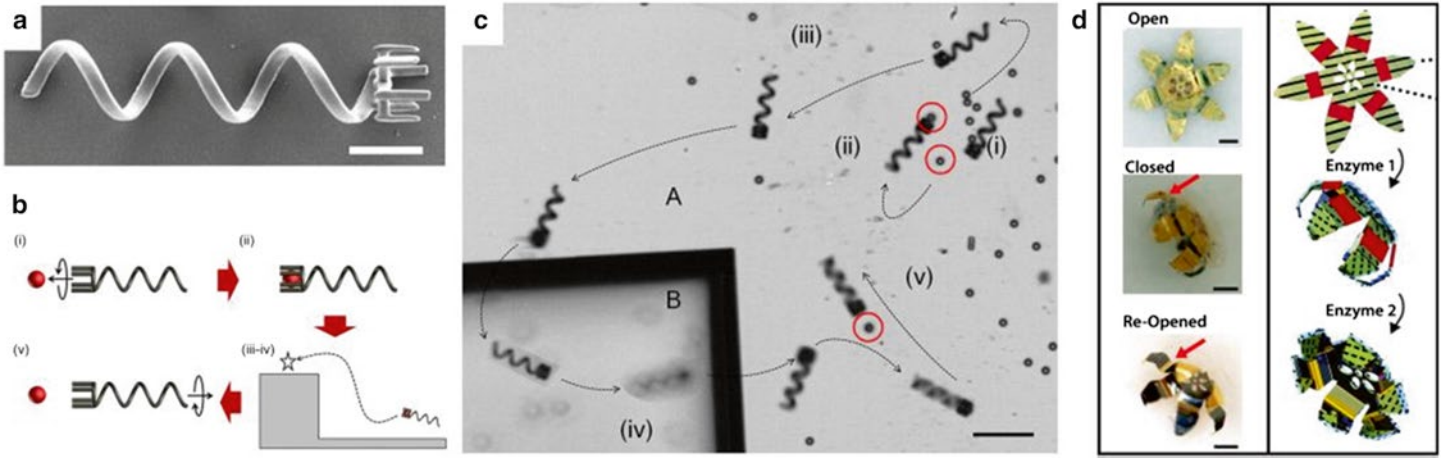

Fig. 9.8 Wirelessly-actuated robotic tools. (**a**) SEM image of a helical micromachine with a hand-like microholder. The scale bar is 10 μm. (**b**) Schematic illustration of cargo transport by the magnetic helical micromachine with a hand-like microholder. (**c**) Time lapse image of transporting 6-μm-diameter microbead in 3D. The scale bar is 50 μm ((**a**–**c**) Adapted with permission from Tottori et al. [41]. Copyright 2012 John Wiley and Sons). (**d**) Biochemically activated microgrippers. The scale bars are 200 μm ((**d**) Adapted with permission from Bassik et al. [78]. Copyright 2010 American Chemical Society)

For microsurgery applications, microtools capable of gripping may be highly useful. Gripping normally requires open-and-close motion of the devices. Based on the development of a micro-origami technique, reconfigurable microgrippers, capable of closing and re-opening wirelessly by external cues, have been fabricated with multilayer flexible joints possessing internal stress [79, 80]. By resolving or altering mechanical property of the reactive layers selectively, the microgrippers can close from a planar shape. Re-opening is also feasible by dissolve the other side of layer with different chemical etchant. A more elegant approach is to engineer the internal or surface stress of the films by biological stimuli. Such kind of autonomous microgrippers are realized recently, e.g. enzyme-responsive microgrippers [78], as shown in Fig. 9.8d. Proteases and glucosidases induce closing and re-opening, respectively. Remote motion control of the microgrippers integrated with a magnetic film can be done by using external magnets. To improve the positioning precision of miniaturized robotic tools, such as microgrippers, an electromagnetic control system is required. A good example of such an electromagnetic setup is OctoMag, which is capable of performing 5-DOF wireless micromanipulation of magnetic device in a large workspace [81].

9.6 Conclusions and Future Outlook

This chapter addressed the recent development of micro/nanorobots with focus on tetherless actuations for locomotion and/or manipulation. Precise motion control and functionalization of the micro/nanorobots by suitable wireless actuation methods enhances the quality of targeted medical treatments, i.e. high concentrating drug delivery and/or microsurgery with minimal side effects. The micro/nanorobots can also be integrated with in vitro biomedical applications, which may provide an alternative processing procedure in comparison to that of a conventional approach. Further investigations on not only wireless actuation technology but also imaging, biocompatibility, etc, are required in the future for practical medical applications.

References

1. Feynman R (1960) There's plenty of room at the bottom. Caltech's Eng Sci 23:22–36
2. Bhat A (2014) Nanobots: the future of medicine. Int J Manage Eng Sci 5(1):44–49
3. Manjunath A, Kishore V (2014) The promising future in medicine: nanorobots. Biomed Sci 2(2):42–47
4. Popa D (2014) Robust and reliable microtechnology research and education through the mobile microrobotics challenge [competitions]. Robot Autom Mag IEEE 21(1):8–12
5. Rao V (2014) Nanorobots in medicine – a new dimension in bio nanotechnology. Trans Netw Commun 2(2):46–57
6. Thangavel K, Balamurugan A, Elango M et al (2014) A survey on nano-robotics in nanomedicine. J NanoSci NanoTechnol 2(1):525–528

7. Nelson B, Kaliakatsos I, Abbott J (2010) Microrobots for minimally invasive medicine. Annu Rev Biomed Eng 12:55–85
8. Patel G, Patel G, Patel R et al (2006) Nanorobot: a versatile tool in nanomedicine. J Drug Target 14(2):63–67
9. Tibbals H (2010) Medical nanotechnology and nanomedicine. CRC Press, Boca Raton
10. Vogel V (2009) Nanotechnology. Nanomedicine, vol 5. Wiley-VCH, Weinheim
11. Campuzano S, Kagan D, Orozco J et al (2011) Motion-driven sensing and biosensing using electrochemically propelled nanomotors. Analyst 136(22):4621–4630
12. Whitesides G (2006) The origins and the future of microfluidics. Nature 442(7101):368–373
13. Dobson J (2006) Magnetic nanoparticles for drug delivery. Drug Dev Res 67(1):55–60
14. Pankhurst Q, Connolly J, Jones S et al (2003) Applications of magnetic nanoparticles in biomedicine. J Phys D Appl Phys 36(13):R167–R181
15. Dames P, Gleich B, Flemmer A et al (2007) Targeted delivery of magnetic aerosol droplets to the lung. Nat Nanotechnol 2(8):495–499
16. Torchilin V (2000) Drug targeting. Eur J Pharm Sci 11:S81–S91
17. Arbab A, Jordan E, Wilson L et al (2004) In vivo trafficking and targeted delivery of magnetically labeled stem cells. Hum Gene Ther 15(4):351–360
18. Wilson M, Kerlan R, Fidelman N et al (2004) Hepatocellular carcinoma: regional therapy with a magnetic targeted carrier bound to doxorubicin in a dual MR imaging/conventional angiography suite – initial experience with four patients. Radiology 230(1):287–293
19. Chertok B, David A, Yang V (2010) Polyethyleneimine-modified iron oxide nanoparticles for brain tumor drug delivery using magnetic targeting and intra-carotid administration. Biomaterials 31(24):6317–6324
20. Liu H, Hua M, Yang H (2010) Magnetic resonance monitoring of focused ultrasound/magnetic nanoparticle targeting delivery of therapeutic agents to the brain. Proc Natl Acad Sci U S A 107(34):15205–15210
21. Yellen B, Forbes Z, Halverson D et al (2005) Targeted drug delivery to magnetic implants for therapeutic applications. J Magn Magn Mater 293(1):647–654
22. Aviles M, Ebner A, Ritter J (2008) Implant assisted-magnetic drug targeting: comparison of in vitro experiments with theory. J Magn Magn Mater 320(21):2704–2713
23. Chorny M, Fishbein I, Yellen B et al (2010) Targeting stents with local delivery of paclitaxel-loaded magnetic nanoparticles using uniform fields. Proc Natl Acad Sci U S A 107(18):8346–8351
24. Kempe H, Kempe M, Snowball I et al (2010) The use of magnetite nanoparticles for implant-assisted magnetic drug targeting in thrombolytic therapy. Biomaterials 31(36):9499–9510
25. Pislaru S, Harbuzariu A, Gulati R et al (2006) Magnetically targeted endothelial cell localization in stented vessels. J Am Coll Cardiol 48(9):1839–1845
26. Polyak B, Fishbein I, Chorny M et al (2008) High field gradient targeting of magnetic nanoparticle-loaded endothelial cells to the surfaces of steel stents. Proc Natl Acad Sci U S A 105(2):698–703
27. Vartholomeos P, Fruchard M, Ferreira A et al (2011) MRI-guided nanorobotic systems for therapeutic and diagnostic applications. Annu Rev Biomed Eng 13:157–184
28. Mathieu J, Martel S (2010) Steering of aggregating magnetic microparticles using propulsion gradients coils in an MRI scanner. Magn Reson Med 63(5):1336–1345
29. Pouponneau P, Leroux J, Martel S (2009) Magnetic nanoparticles encapsulated into biodegradable microparticles steered with an upgraded magnetic resonance imaging system for tumor chemoembolization. Biomaterials 30(31):6327–6332
30. Pouponneau P, Leroux J, Soulez G et al (2011) Co-encapsulation of magnetic nanoparticles and doxorubicin into biodegradable microcarriers for deep tissue targeting by vascular MRI navigation. Biomaterials 32(13):3481–3486
31. Riegler J, Wells J, Kyrtatos P et al (2010) Targeted magnetic delivery and tracking of cells using a magnetic resonance imaging system. Biomaterials 31(20):5366–5371
32. Ludwig W (1930) Zur theorie der flimmerbewegung (Dynamik, Nutzeffekt, Energiebilanz). Physiol 13:397–504

33. Purcell E (1977) Life at low Reynolds-number. Am J Phys 45(1):3–11
34. Dreyfus R, Baudry J, Roper M et al (2005) Microscopic artificial swimmers. Nature 437(7060):862–865
35. Fischer P, Ghosh A (2011) Magnetically actuated propulsion at low Reynolds numbers: towards nanoscale control. Nanoscale 3(2):557–563
36. Gao W, Sattayasamitsathit S, Manesh K et al (2010) Magnetically powered flexible metal nanowire motors. J Am Chem Soc 132(41):14403–14405
37. Ghosh A, Fischer P (2009) Controlled propulsion of artificial magnetic nanostructured propellers. Nano Lett 9(6):2243–2245
38. Peyer K, Tottori S, Qiu F et al (2013) Magnetic helical micromachines. Chem Eur J 19(1):28–38
39. Qiu F, Zhang L, Tottori S et al (2012) Bio-inspired microrobots. Mater Today 15(10):463
40. Tottori S, Sugita N, Kometani R et al (2011) Selective control method for multiple magnetic helical microrobots. J Micro-Nano Mech 6(3–4):89–95
41. Tottori S, Zhang L, Qiu F et al (2012) Magnetic helical micromachines: fabrication, controlled swimming, and cargo transport. Adv Mater 24(6):811–816
42. Zhang L, Abbott J, Dong L et al (2009) Artificial bacterial flagella: fabrication and magnetic control. Appl Phys Lett 94(6):064107
43. Zhang L, Abbott J, Dong L et al (2009) Characterizing the swimming properties of artificial bcterial flagella. Nano Lett 9(10):3663–3667
44. Zhang L, Peyer KE, Nelson B (2010) Artificial bacterial flagella for micromanipulation. Lab Chip 10(17):2203–2215
45. Schmidt O, Eberl K (2001) Nanotechnology – thin solid films roll up into nanotubes. Nature 410(6825):168
46. Zhang L, Ruh E, Grützmacher D (2006) Anomalous coiling of SiGe/Si and SiGe/Si/Cr helical nanobelts. Nano Lett 6(7):1311–1317
47. Hawkeye M, Brett M (2007) Glancing angle deposition: fabrication, properties, and applications of micro- and nanostructured thin films. J Vac Sci Technol A 25(5):1317–1335
48. Peyer K, Zhang L, Nelson B (2011) Localized non-contact manipulation using artificial bacterial flagella. Appl Phys Lett 99(17):174101
49. Peyer K, Zhang L, Nelson B (2013) Bio-inspired magnetic swimming microrobots for biomedical applications. Nanoscale 5(4):1259–1272
50. Abbott J, Peyer K, Lagomarsino M et al (2009) How should microrobots swim? Int J Robot Res 28(11–12):1434–1447
51. Behkam B, Sitti M (2006) Design methodology for biomimetic propulsion of miniature swimming robots. J Dyn Syst-T ASME 128(1):36–43
52. Blakemore R (1975) Magnetotactic bacteria. Science 190(4212):377–379
53. Martel S, Mohammadi M, Felfoul O et al (2009) Flagellated magnetotactic bacteria as controlled MRI-trackable propulsion and steering systems for medical nanorobots operating in the human microvasculature. Int J Robot Res 28(4):571–582
54. Martel S, Tremblay C, Ngakeng S et al (2006) Controlled manipulation and actuation of micro-objects with magnetotactic bacteria. Appl Phys Lett 89(23)
55. Weibel D, Garstecki P, Ryan D et al (2005) Microoxen: microorganisms to move microscale loads. Proc Natl Acad Sci U S A 102(34):11963–11967
56. Martel S, Mohammadi M (2010) Using a swarm of self-propelled natural microrobots in the form of flagellated bacteria to perform complex micro-assembly tasks. Paper presented at the IEEE International Conference on Robotics and Automation (ICRA), May
57. Steager E, Kim C, Patel J et al (2007) Control of microfabricated structures powered by flagellated bacteria using phototaxis. Appl Phys Lett 90(26):263901
58. Paxton W, Kistler K, Olmeda C et al (2004) Catalytic nanomotors: autonomous movement of striped nanorods. J Am Chem Soc 126(41):13424–13431
59. Fournier-Bidoz S, Arsenault A, Manners I et al (2005) Synthetic self-propelled nanorotors. Chem Commun 4:441–443

60. Gibbs J, Zhao Y (2011) Catalytic nanomotors: fabrication, mechanism, and applications. Front Mater Sci 5(1):25–39
61. Mei Y, Solovev A, Sanchez S et al (2011) Rolled-up nanotech on polymers: from basic perception to self-propelled catalytic microengines. Chem Soc Rev 40(5):2109–2119
62. Mirkovic T, Zacharia N, Scholes G et al (2010) Fuel for thought: chemically powered nanomotors out-swim nature's flagellated bacteria. ACS Nano 4(4):1782–1789
63. Wang J (2009) Can man-made nanomachines compete with nature biomotors? ACS Nano 3(1):4–9
64. Solovev A, Sanchez S, Pumera M et al (2010) Magnetic control of tubular catalytic microbots for the transport, assembly, and delivery of micro-objects. Adv Funct Mater 20(15):2430–2435
65. Sanchez S, Solovev A, Schulze S et al (2011) Controlled manipulation of multiple cells using catalytic microbots. Chem Commun 47(2):698–700
66. Kagan D, Campuzano S, Balasubramanian S et al (2011) Functionalized micromachines for selective and rapid isolation of nucleic acid targets from complex samples. Nano Lett 11(5):2083–2087
67. Gao W, Sattayasamitsathit S, Orozco J et al (2011) Highly efficient catalytic microengines: template electrosynthesis of polyaniline/platinum microtubes. J Am Chem Soc 133(31):11862–11864
68. Burdick J, Laocharoensuk R, Wheat P et al (2008) Synthetic nanomotors in microchannel networks: directional microchip motion and controlled manipulation of cargo. J Am Chem Soc 130(26):8164–8165
69. Kagan D, Laocharoensuk R, Zimmerman M et al (2010) Rapid delivery of drug carriers propelled and navigated by catalytic nanoshuttles. Small 6(23):2741–2747
70. Sundararajan S, Sengupta S, Ibele M et al (2010) Drop-off of colloidal cargo transported by catalytic Pt-Au nanomotors via photochemical stimuli. Small 6(14):1479–1482
71. Balasubramanian S, Kagan D, Hu C et al (2011) Micromachine-enabled capture and isolation of cancer cells in complex media. Angew Chem Int Edit 50(18):4161–4164
72. Orozco J, Campuzano S, Kagan D et al (2011) Dynamic isolation and unloading of target proteins by aptamer-modified microtransporters. Anal Chem 83(20):7962–7969
73. Campuzano S, Orozco J, Kagan D et al (2012) Bacterial isolation by lectin-modified microengines. Nano Lett 12(1):396–401
74. Kagan D, Calvo-Marzal P, Balasubramanian S et al (2009) Chemical sensing based on catalytic nanomotors: motion-based detection of trace silver. J Am Chem Soc 131(34):12082–12083
75. Wu J, Balasubramanian S, Kagan D et al (2010) Motion-based DNA detection using catalytic nanomotors. Nat Commun 1
76. Ozin G, Manners I, Fournier-Bidoz S et al (2005) Dream nanomachines. Adv Mater 17(24):3011–3018
77. Leong T, Zarafshar A, Gracias D (2010) Three-dimensional fabrication at small size scales. Small 6(7):792–806
78. Bassik N, Brafman A, Zarafshar A et al (2010) Enzymatically triggered actuation of miniaturized tools. J Am Chem Soc 132(46):16314–16317
79. Leong T, Randall C, Benson B et al (2009) Tetherless thermobiochemically actuated microgrippers. Proc Natl Acad Sci U S A 106(3):703–708
80. Randhawa J, Leong T, Bassik N et al (2008) Pick-and-place using chemically actuated microgrippers. J Am Chem Soc 130(51):17238–17239
81. Kummer M, Abbott J, Kratochvil B (2006) An electromagnetic system for 5-DOF wireless micromanipulation, IEEE. Trans Robot 26(6):1006–1017